Magnetic Resonance Navigation of a Bead Inside a Three-Bifurcation PMMA Phantom Using an Imaging Gradient Coil Insert

Alexandre Bigot, Charles Tremblay, Gilles Soulez, and Sylvain Martel, *Senior Member, IEEE*

***Abstract*—This paper reports the successful navigation of a 1-mm Chrome-Steel bead along three consecutive polymethyl methacrylate channels inside the bore of a 1.5-T magnetic resonance imaging (MRI) scanner. The bead traveled at a mean velocity of 14 cm·s^{-1}. This was accomplished using an imaging gradient coil (IGC) insert located inside the MRI tube. While targeting one side of a bifurcation has been previously demonstrated using unidirectional gradient coils, this is the first time that magnetic resonance navigation (MRN) of a bead along consecutive channels is reported. Experimental results confirm that a clinical regular MRI can be used to propel a 1-mm device. In addition, when used at maximum power, IGC temperature rise becomes a serious issue that can ultimately damage the insert and limit the overall performance. Consequently, this paper aims to give some insight into coil temperature management for IGC-assisted procedures. A 33-min thermal stress test was carried out using 100% of the IGC power. Steady-state oscillation can be reached by interleaving propulsion periods with cooling periods, thus enabling longer propulsion procedures. Experimental data showed that the cooling time can be used for imaging purposes with no performance loss, thus enabling MRN-assisted procedures with multiplexed particle distribution assessment.**

***Index Terms*—Imaging gradient coil (IGC), magnetic resonance navigation (MRN), magnetic targeting, medical robots and systems, multiple bifurcation navigation, temperature behavior.**

I. Introduction

With the recent development of high-demanding imaging techniques such as diffusion tensor imaging (DTI), new boosted imaging hardwares are being developed in order to get faster, shorter, and higher resolution imaging sequences for magnetic resonance imaging (MRI) [1]–[3]. To achieve high performance and reduce the overall cost, such a system usually consists of coil inserts that can be mounted in the bore of an MRI [4]–[6]. Gradient inserts have several advantages compared to regular human-sized coil: high magnetic gradients, high slew rate, and lower cost. Although the design of such insert coils is oriented toward better imaging performance, it may also lead to a huge improvement in magnetic resonance navigation (MRN) [5], [7].

MRN is a fairly new technique which exploits both the high magnetic field of an MRI scanner and the magnetic gradients generated by a coil to steer a carrier vehicle embedding a functional drug inside the human vessel network [7], [8]. Such technology is a promising research area which aims at improving the localized delivery of theranostics agents toward a disease region of the body while maintaining low systemic drug concentration (see Fig. 1). MRN can potentially improve therapies such as liver and brain chemoembolization by serially navigating single boluses to a disease site to reach a given dose locally [9], [10]. More than a steering actuator, MRI also enables particle tracking and particle distribution evaluation during the procedure [11]. Polymer particles embedding doxorubicin as a therapeutic agent, dubbed therapeutic magnetic microcarriers, have already been successfully synthesized and steered in a rabbit liver using a

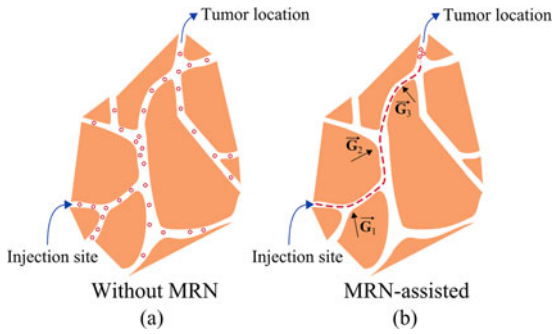

Fig. 1. Representation of a vascular network. Empty circles are microvectors embedding imaging or therapeutic agents. (a) Current chemoembolization procedure is done by injecting chemotherapeutic drug from a catheter—the injection site—toward a tumor with no control over the injected particles. (b) By correctly applying consecutive magnetic gradients $\mathbf{G}_1$, $\mathbf{G}_2$, and $\mathbf{G}_3$, MRN-assisted chemoembolization could potentially enable the control of the injected vectors to serially navigate them from the injection site toward the disease site (dashed line), thus preserving parenchyma healthy tissues.

Manuscript received August 9, 2013; revised December 2, 2013; accepted January 13, 2014. This work was supported by the Research Chair of Polytechnique Montreal in Nanorobotics and grant from the National Sciences and Engineering Research Council of Canada (NSERC). The equipment used in this study was acquired with a grant from the Canada Foundation for Innovation (CFI). This paper was recommended for publication by Editor Bradley J. Nelson upon evaluation of the reviewers' comments.

A. Bigot is with the NanoRobotics Laboratory, Department of Computer and Software Engineering and Institute of Biomedical Engineering, École Polytechnique de Montréal (EPM), Montreal, QC H3T 1J4, Canada, and the Department of Radiology, Centre Hospitalier de l'Université de Montréal, Montreal, QC H3T 1C5, Canada (e-mail: alexandre.bigot@polymtl.ca).

C. Tremblay and S. Martel are with the NanoRobotics Laboratory, Department of Computer and Software Engineering and Institute of Biomedical Engineering, École Polytechnique de Montréal (EPM), Montréal, QC H3T 1J4, Canada (e-mail: ctremblay@polymtl.ca; sylvain.martel@polymtl.ca).

G. Soulez is with the Centre Hospitalier de l'Université de Montréal, Department of Radiology, Montreal, QC H3T 1C5, Canada (e-mail: gilles.soulez.chum@ssss.gouv.qc.ca).

This paper has supplementary downloadable material available at http://ieeexplore.ieee.org, provided by the authors.

Color versions of one or more of the figures in this paper are available online at http://ieeexplore.ieee.org.

Digital Object Identifier 10.1109/TRO.2014.2300591

400 mT·m^{-1} unidirectional gradient coil and T2*-weighted MR images for particle distribution assessment [12].

The ability to steer microrobots inside the small human blood vessels requires highly specialized systems to navigate through the winding architecture of vessels [13]–[15]. Currently, two different approaches to propel microrobots using magnetic fields exist: low-magnetic field strength environments [16], [17] and high-magnetic field strength environments [18], [19]. The former approach usually has a high number of degree of freedom (DOF) which provides high accuracy and, therefore, is suitable for precise microsurgical procedures. However, it has serious constraints on the medical procedures that can be performed because of limited induced force on the propelled body and to the rapid decay of the magnetic force.

The latter approach, referred to as MRN, has only 3-DOF but does not suffer from the magnetic force decay. Besides, the high-magnetic-field environment ensures high magnetization and, consequently, high-induced magnetic force on the bead, suitable for endovascular navigation. However, it requires high performance—namely ultrahigh amplitude gradient and low switching times (low rise time and fall time)—coil assembly. A 400 mT·m^{-1} steering gradient coil (SGC) has proven to be effective for magnetic catheter steering [20] or single bifurcation liver targeting [9], but it does not exhibit sufficient performance to perform MRN in tiny vessel networks such as deep liver vasculature or brain vasculature due to a high switching time [21]. While the state of power amplifier technology was used to limit the maximum gradient performance in the past, development of imaging inserts leads to broad availability of imaging gradient coil (IGC) systems which can exhibit gradient strength of several hundreds of millitesla per meter and high slew rates [3], [6]. Such systems have a reduced diameter to generate ultrahigh gradient strength thus limiting MRN to limbs, head, and small animals. However, Kimmlingen *et al.* worked on the human-sized 400 mT·m^{-1} imaging coil prototype for DTI whose performance could make whole-body MRN feasible [22]. With this new available hardware, custom three-dimensional (3-D) gradient sequences can be easily designed, and such performance may open the way to multiple bifurcation navigation of ferromagnetic beads.

Contrary to SGC, which is specifically designed for propulsion and thus can be operated in dc-mode [23], IGC suffers from temperature rise when both high duty cycle and high-amplitude gradients are required. The duty cycle, defined as the ratio of the operating time over the total period, is an important figure of merit to evaluate MRN performance. Imaging routines have generally low duty cycle gradients. Hence, such sequences are not very demanding and thus do not induce any temperature increase of the tube. On the other hand, propulsion sequences require maximum magnetic gradient strength—ten times higher than regular MRI gradients—with high slew rate and maximum duty cycle. Such gradient configuration requires much power and thus generates a lot of heat in the insert. Without sufficient cooling, uncontrolled temperature rise could lead to system failure. Therefore, using an IGC for imaging purposes is very different than using it for propulsion purposes, and stress testing such high-power system in MRN mode is mandatory

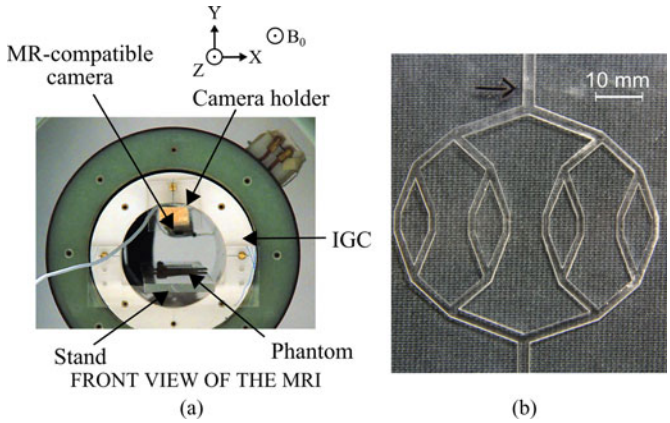

Fig. 2. (a) Front view of the propulsion setup located inside the bore of a 1.5T MRI. The phantom is located at the middle of the IGC, with the camera on top of it. The B_0 field of the MRI is along $+$Z. (b) Top view of the phantom used for the navigation experiments. The black arrow indicates the initial position of the bead.

to verify proper functionality and assess the overall efficiency of IGC-assisted MRN. Management of temperature is therefore among the current challenges of MRN in tiny vessels [21].

Aside from heating considerations, whereas IGC exhibits performance for multiple bifurcation MRN, it has yet to be demonstrated. Therefore, this paper is a proof of concept that magnetic bodies can be propelled through several consecutive branches *in vitro* using an IGC. We designed and built a polymethyl methacrylate (PMMA) phantom with multiple bifurcations to perform navigation tests. From the gathered data, we then verified that the system can sustain a whole propulsion procedure where thousands of boluses are serially navigated. Data analysis of this stress test provides useful information to optimize MRN procedures and build a theoretical framework for any navigation experiment.

The paper is organized as follows: first, an MRN experiment is conducted inside a multiple bifurcation phantom. Then, a stress test is performed on the coil to check whether it could sustain a whole MRN-assisted procedure for several minutes. Finally, some strategies are presented in order to optimize the overall procedure efficiency. These results fall within the context of targeted therapies where untethered endovascular devices embedding chemotherapeutic drugs are navigated toward a tumor site.

II. Material and Methods

The test bench is composed by a multiple bifurcation phantom, an MR-compatible camera and a 1-mm bead carefully placed at the center of a shielded BFG-240/150-S-7 micro-IGC (Resonance Research, Inc., USA). The coil is connected to a Neslab Heat Exchanger II which provides 4.8 l/ min of constant 15 °C cooling water. A photograph of the MRN setup is shown in Fig. 2(a).

The whole setup is inserted inside the bore of a clinical MRI scanner (Siemens Sonata 1.5T, Germany). Its high permanent magnetic field ensures high level of magnetization and, thus, maximum steering force [19]. The phantom is made of two

TABLE I
GEOMETRIC CHARACTERISTICS OF THE PHANTOM

Level	L [mm]	W [mm]	Depth [mm]	$\theta_{i,i+1}$ [°]	θ_i [°]
Root	3.2	2.6	1.5	110	140
1	16.64	2.16		62	97
2	11.15	1.8		109	44
3	10.05	1.68		-	160

PMMA plates thermally bonded together. Additional details about the phantom are given in the next section. Videos were recorded using the 12M MRC MR-Compatible Camera (MRC Systems GmbH, Germany) at 28 frames/s. The camera was set above the setup, as close as possible to the IGC inner top surface to get maximum field of view (FOV).

The navigated bead is 1 mm in diameter and is made of Chrome-Steel (Salem Specialty Ball). Its magnetization at saturation is $M_{\text{sat}} = 1.44 \times 10^6$ A·m^{-1}. Custom propulsion and imaging sequences were designed using TNMR (TECMAG, USA) v. 2.11.2 software and triggered using a 5-V transistor–transistor-logic pulse generated by an Agilent 33220A signal generator.

A. Multiple Bifurcation Navigation

In vitro single bifurcation MR-steering has already been demonstrated by Mathieu *et al.* and Pouponneau *et al.* [8], [9], [19]. At that time, actuator characteristics—unidirectional 400 mT·m^{-1} coils—did not allow multiple bifurcation navigation. The state-of-the-art gradient coils now exhibit 3-D dynamic and static performance that could potentially make multiple bifurcation navigation feasible.

To perform such a test, we built a symmetric transparent PMMA phantom (length: 14.5 cm; width: 9 cm; depth: 0.3 cm) mimicking an arterial tree as shown in Fig. 2(b). Channel widths and depths (see Table I) were chosen to allow bead navigation and proper visualization with the reduced FOV of the MR-compatible camera.

The phantom was filled with deionized water and bubbles were evacuated using high-pressure pump. When all the bubbles were out of the circuit, the two ends of the phantom were connected together using a three-way valve. The phantom was then placed inside the linear gradient volume of the insert on the xz plane (coronal plane of the MRI), as depicted in Fig. 2(a).

For a duty cycle of 1, considering a microparticle of volume V at constant volume magnetization $\boldsymbol{M}_{\mathbf{sat}}$ in an MRI magnetic field $\boldsymbol{B} = B_0\boldsymbol{z}$, the magnetic force is given by [21]:

$$\boldsymbol{F}_{\text{mag}} = VM_{\text{sat}}\mathbf{G} \tag{1}$$

where $\mathbf{G}$ the gradient vector defined as $\mathbf{G} = [\frac{\partial \text{B}_\text{z}}{\partial \text{x}}; \frac{\partial \text{B}_\text{z}}{\partial \text{y}}; \frac{\partial \text{B}_\text{z}}{\partial \text{z}}]$. Consequently, the x-gradient is responsible for the bead steering, the y-gradient is used to counteract the gravity, and as no flow is present, the z-gradient is responsible for the bead thrust.

Phantom channels have been divided into four levels: root level, level 1, level 2, and level 3 [see Fig. 3(a)]. At each level, branches are lettered $+$ and $-$, according to the gradient axis depicted on the top-left corner of Fig. 3(b). For instance, to reach the third channel from the left of level 3, the gradient sequence would be $-+-$. The objective is to navigate the bead from the root channel to all of the level 3 channels using the following eight gradient sequences : $---$; $--+$; $-+-$; $-++$; $+--$; $+-+$; $++-$; $+++$.

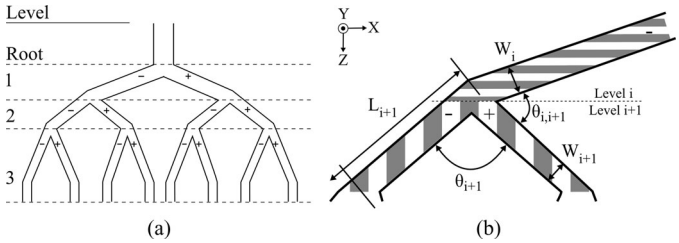

Fig. 3. (a) Schematic of the phantom with respective levels. Root channel is the starting branch. Then at each level, two paths can be chosen: either $+$ or $-$ according the gradient directions depicted at the top-right. Any navigation path from root level to level 3 thus exhibits three branch splits. (b) Geometric features of PMMA multiple-bifurcation phantom. The parent branch (level i, horizontal stripes) splits into two child branches (level $i+1$, vertical stripes). The two child branches are either referred as $+$ or $-$ according to the x-axis sign. L and W are, respectively, the length and the width of a channel. θ_i is the angle between $+$ and $-$ branches, and $\theta_{i,i+1}$ is the inner angle between the parent branch and the child branch.

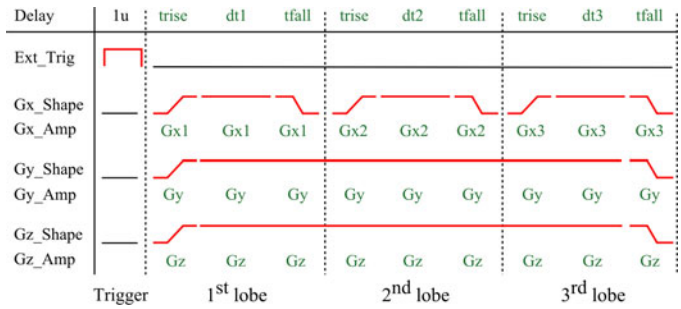

Fig. 4. Custom propulsion sequence is made of four events: trigger, first lobe, second lobe, and third lobe. The triggering event is used to synchronize the gradient pulse application with the video recording. A gradient pulse is defined by its shape (Shape line) and its amplitude (Amp line). A pulse has three events: a rising edge (of duration t_{rise}), a plateau (of duration $\text{d}t_i$), and a falling edge (of duration t_{fall}). The event amplitude can be either positive or negative. When no amplitude is defined, the gradient is zero. Rise time (t_{rise}) and fall time (t_{fall}) are set to 5 ms. Each gradient lobe i has a plateau duration of $\text{d}t_i$. Symbols "u" and "m" stand for microseconds and milliseconds, respectively.

A typical propulsion sequence is depicted in Fig. 4. It can be divided into four sections: trigger, first bifurcation, second bifurcation, and third bifurcation. The trigger event is used to synchronize the sequence with the video recording. Afterwards, the x-gradient G_X is switched ON and OFF three times at decreasing durations dt1, dt2, and dt3, and at amplitude G_{X1}, G_{X2}, and G_{X3} according to phantom characteristics.

B. Heating Protocol

During a regular medical procedure, several milliliters of therapeutic particles need to be injected in order to reach the required therapeutic drug dose. Navigation of such agents requires the injection of consecutive boluses that will be serially steered from the injection site—the tip of the catheter—to the target location. Consequently, MRN-based procedures require as many propulsion sequences as the number of boluses that needs to be injected. Therefore, theoretically, the overall procedure time is

TABLE II
HEATING SEQUENCE PARAMETERS

Pulse number	Duration [ms]	G_X amplitude [T·m^{-1}]	G_Y amplitude [T·m^{-1}]	G_Z amplitude [T·m^{-1}]
1	160	+0.324 (100%)	0	0
2	85	−0.325 (100%)		
3	50	+0.324 (100%)		
4	74	0		

Values in parenthesis relate to the maximum gradient amplitude the IGC can produce.

TABLE III
PROPULSION SEQUENCE PARAMETERS FOR BRANCHING PATTERN $+ - +$

Pulse number	Duration [ms]	G_X amplitude [T·m^{-1}]	G_Y amplitude [T·m^{-1}]	G_Z amplitude [T·m^{-1}]
1	160	+0.026 (8%)	+0.064 (20%)	+0.0285 (9%)
2	85	−0.026 (8%)		
3	50	+0.026 (8%)		

Values in parenthesis relate to the maximum gradient amplitude the IGC can generate.

equal to the time to inject plus the time to navigate the bolus times the number of boluses to be injected. However, recent experimental data showed that temperature is clearly an issue when IGC is used for propulsion and severely limits MRN performance. We therefore have designed and performed a stress test on the IGC which would reproduce a MRN-assisted procedure to evaluate the overall performance.

We assumed a similar branching configuration as that in the PMMA phantom experiment: all vessels lay in the *xz* plane (coronal plane) and vessel characteristics are the same as in the phantom. Additionally, injected particles will be carried by the blood, and thus, no y- and z-gradients are required to induce bead movement. In addition, we assume the targeted area is located three bifurcations away from location of the injection and can be reached with the steering pattern $+ - +$ using maximum x-gradient amplitude. Finally, to take into account the dead time between injections of boluses, we added a resting time of 74 ms where no gradients are applied. Hence, the duty cycle of the gradient sequence, referred as D_{sequence}, is 80%. The summary of the MRN sequence parameters is given in the Table II.

The stress test protocol is the following: the procedure is initiated when the internal coil temperature is 30 °C and keeps running until the temperature reaches 50 °C. At 50 °C, all the pulses are stopped and the coil is let to cool until its temperature returns to 45 °C and then the sequence is started again. After five iterations, the stress test is stopped and the coil is allowed to cool down to its idle temperature.

Using IGC characteristic temperature curves for a duty cycle of 80%, this sequence should allow around 30 s of propulsion and will require around 293 s of cooling to go down to 45 °C. The expected duty cycle of the procedure, referred as $D_{\mathrm{procedure}}$, is therefore 8%.

III. RESULTS

A. Navigation of Bead Inside a Phantom

The 1-mm bead was successfully navigated in all the eight branching patterns, as shown in the supplementary video. The video footage was not accelerated and navigation is shown at real speed. While the navigation time is short, the overall experiment lasted around 1 h because of the trial and error method. With sufficient expertise and training, the time needed to test the eight navigation paths can be severely reduced to a few minutes. The applied gradient parameters are given in Table III. Fig. 5 gives an example of navigation footage and its associated gradient pulses.

To induce bead movement and make the bead visible on the footage, the G_Z amplitude is set to 28.5 mT·m^{-1}. G_Y is set to 64 mT·m^{-1} to lift the bead. Finally, x-gradient parameters—amplitude and durations—are adjusted according to the phantom geometrical features and angles between channels (see Table I). Selection of a navigation path is made by changing the sign of the x-gradient pulses.

The velocity can be estimated by three means: from magnetic equations (see the Appendix), from sequence parameters (see Table III) and phantom geometric characteristics (see Table I), and from the video footage.

From the gradient total duration (295 ms) and the total travel length (41 mm), the mean velocity is found to be 0.14 m·s^{-1} which is in agreement with the theoretical mean velocity of the bead over 295 ms of navigation that is found to be $v_{\mathrm{mean}} = \sqrt{(v_{\mathrm{mean}^x})^2 + (v_{\mathrm{mean}^z})^2} = 0.143$ m·s^{-1} (see the Appendix).

The bead velocity from the video footage—41 mm in 12 navigation frames at 29 frames/s yields a mean velocity of 0.099 m·s^{-1}—is underestimated because the number of frames per second is not high enough to precisely extract the duration of the navigation.

B. Heating Experiment

Results of the stress test are depicted in the Fig. 6 and reported in Table IV. The experiment lasted 46 min and exhibited five temperature oscillations. Interleaving propulsion periods and cooling periods make the coil inner temperature to oscillate. Both the lowest and the highest temperatures show a steady-state value of $T_{\mathrm{low}} = 42$ °C and $T_{\mathrm{high}} = 55$ °C, respectively, meaning that the experiment could have been carried on over a longer period of time, for instance, to reach a higher number of injected particles. As reported in Table IV, the mean propulsion time t_{ON} is 83 s and the mean cooling time t_{OFF} is 301 s. In addition, temperature curve shows both temperature overshoot and temperature lag due to the location of temperature sensors on the coil.

The following linear model was used to model the temperature oscillations:

$$T(t) = \begin{cases} \alpha_{\mathrm{heat}} t + T_{\mathrm{low}}, & \text{heating period} \\ -\alpha_{\mathrm{cool}} t + T_{\mathrm{high}}, & \text{cooling period} \end{cases} \quad (2)$$

where α is a rate constant depending on the state of the coil—heating or cooling. Results of linear data fitting are reported in Table IV and superimposed on the temperature plot in Fig. 6.

Interestingly, one can observe that the first heating period has a heating rate constant $\alpha_{\mathrm{heat}} = 10.8$ °C·min^{-1}. However, subsequent pulses show a heating rate constant around 7.4 °C·min^{-1}, meaning that the coil temperature increase is slower at high

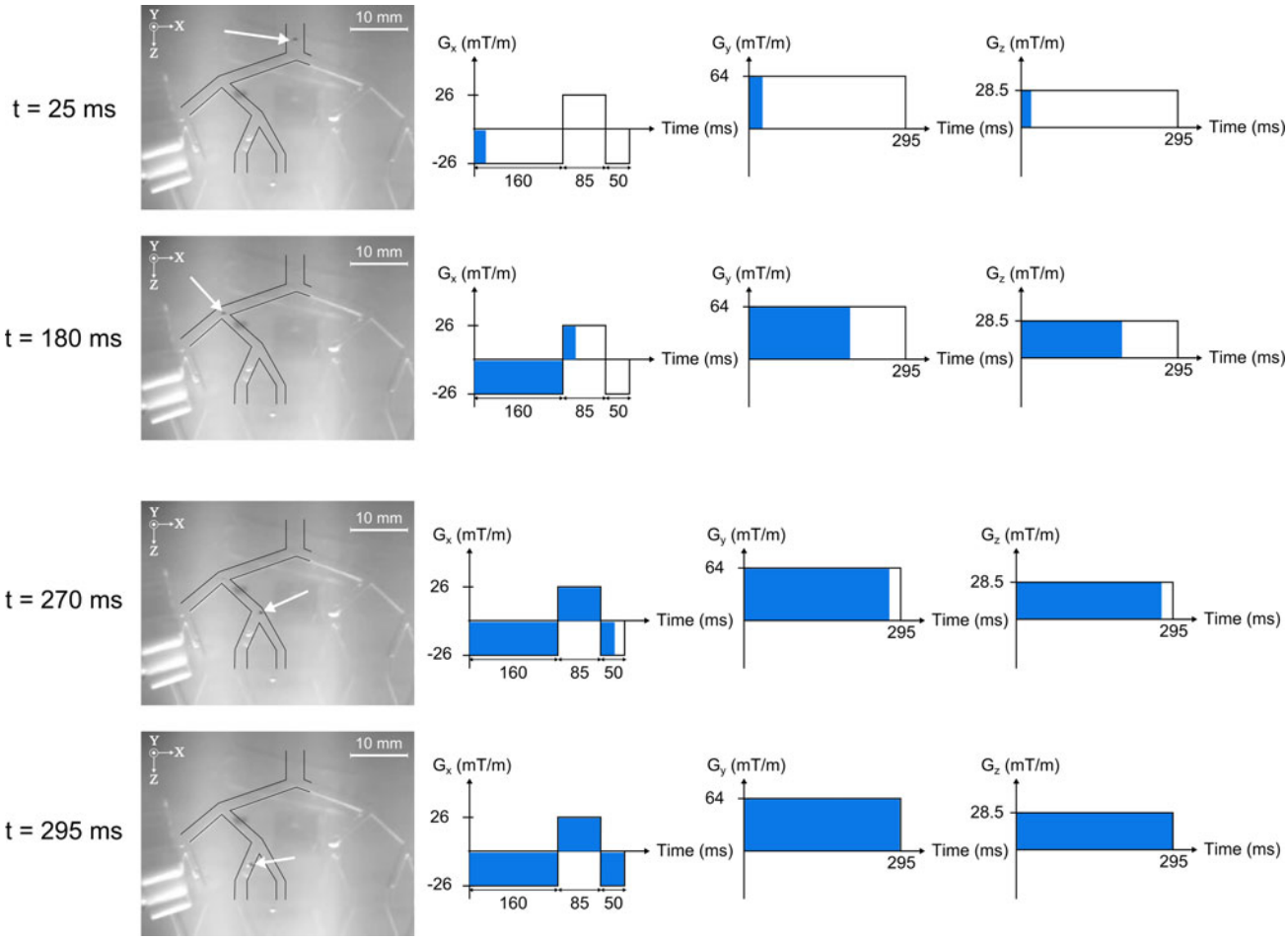

Fig. 5. Each row represents a different video time frame for the propulsion sequence $-+-$. The first column contains raw images of the footage. Arrows indicate the bead location and the black lines indicate the edges of the channel. The second column schematically depicts the evolution and the current state (blue coloring) of x-, y-, and z-gradients at the corresponding video frame. The directions of the gradients are shown in the top-left corner of the video frames. Additional details on the timing and amplitude values of the gradients are given in Section III.

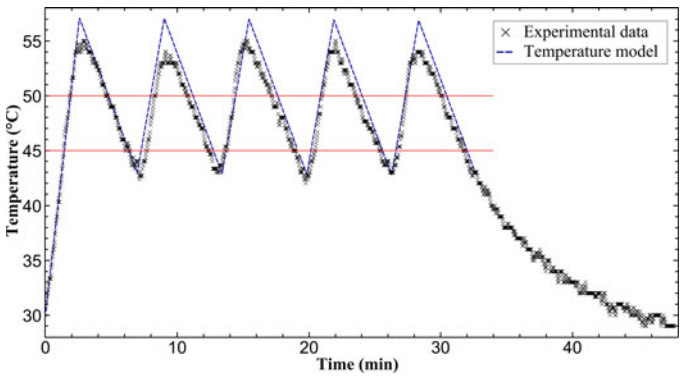

Fig. 6. Evolution of the IGC temperature over time. Data are plotted every 5 s and have been smoothed using a moving average filter. A linear model is plotted in a dashed line. Experiment lasted 46 min in total. Oscillating pattern shows around 83 s of navigation and 301 s of cooling time. The two horizontal plain lines represent the 50 °C-temperature threshold when the pulses were stopped and the 45 °C-temperature threshold when the pulses were started.

TABLE IV
RESULTS OF THE STRESS TEST

Pulse number	t_{ON} [s]	t_{OFF} [s]	T_{low} [°C]	T_{high} [°C]	α_{heat} [°C·min^{-1}]	α_{cool} [°C·min^{-1}]
1	148 (155)	303 (263)	30 (30.0)	55 (57.1)	10.8 (10.5)	3.17 (3.24)
2	82 (124)	279 (263)	42 (42.9)	54 (57.2)	7.2 (6.9)	3.16 (3.24)
3	85 (124)	315 (263)	42 (43.0)	55 (57.0)	7.3 (6.9)	2.84 (3.24)
4	83 (124)	300 (263)	42 (42.8)	55 (57.0)	7.7 (6.9)	2.77 (3.24)
5[2]	82 (124)	306 (263)	43 (42.8)	54 (56.9)	7.4 (6.9)	2.95 (3.24)
Mean[1]	83 (124)	301 (263)	42.3 (42.6)	54.6 (57.0)	7.4 (6.9)	2.98 (3.24)
Sum	480 (651)	1503 (1315)	-	-	-	-

Values in parenthesis are values used for the temperature model.
[1]Excluding 1st heating pulse.
[2]Excluding data from T_{low} to the coil idle temperature.

temperature. This phenomenon can also explain the difference between the expected procedure duty cycle (8%) and the experimental procedure duty cycle (24%): Characteristics curves, which depict only the first heating phase, underestimate the available propulsion time and, thus, the duty cycle. Such considerations are discussed in further detail in the next section.

TABLE V
OVERALL PERFORMANCE OF OUR PROPULSION SETUP

Sequence duration [s]	$D_{sequence}$ [%]	$D_{procedure}$ [%]	Number of injections	Procedure duration [min]
0.369	80	24 (33)	1526 (1764)	33

Values in parenthesis are computed from the temperature model.

For this specific experiment, the total available time for propulsion is 480 s (around 8 min) divided up into five burst-mode pulses. The number of injections per second is 2.7 meaning that near 225 injections are performed during each propulsion pulse. Consequently, 1530 boluses can be injected and navigated along three consecutive channels within 33 min of procedure. Table V gives the overall performance of our setup and our propulsion pattern—three bifurcations, 80% duty cycle.

In the end, careful management of the coil temperature can enable the injection of several consecutive boluses during a potential infinite amount of time. If a higher number of boluses are needed—higher therapeutic dose—the operator can easily use an oscillating temperature approach in order to extend the intervention time and increase the number of delivered microparticles.

IV. DISCUSSION

A. Dynamic Navigation

To our knowledge, this is the first time that an MRN along a path that includes three bifurcations is reported. Results indicate that the maximum number of bifurcations can be increased. Two factors currently limit the maximum number of bifurcations: coil temperature rise whose influence is discussed in the next section, and the limited diameter of spherical volume (DSV). For the BFG-240/150-S-7 imaging coil, the DSV is 8 cm. In comparison, the 1.5T Siemens Sonata MRI has a DSV of 50 cm. Navigation outside this volume is not desirable as gradient amplitude and direction are not properly defined.

While an experiment using a flow mimicking physiologic conditions is obviously more realistic, it adds several challenges and constraints for dynamic MRN in several consecutive channels.

Indeed, since several consecutive gradient pulses are required, a branch can be easily missed if the gradient pulses are turned on too early or too late, therefore reducing the efficiency. Precise synchronization between the bolus position and gradient triggering is mandatory for MRN.

Using a video camera for visual tracking is suitable for trial and error *in vitro* experiments but it is not suitable for *in vivo* experiments. Advanced control methods which rely on MRI-based tracking algorithm exist and they have proven to be adequate to track 1.5-mm beads at a rate of 20 to 30 times per second [7], [11]. While locating particles as small as 15 μm with MRI is feasible [24], the tracking rate is drastically reduced for submillimeter particles and does not allow fast accurate positioning. Therefore, finding an optimal feedback approach is a major challenge in MRN and alternative imaging and control methods must be considered [14], [25], [26].

Extensive work remains to be done to build a 3-D *in vitro* experimental test bench that would reproduce the conditions of endovascular targeting procedure.

B. Oscillation Protocol

Assuming linear temperature behavior, one can derive an expression for the duty cycle depending only on rate coefficients α_{heat} and α_{cool}. Using (1) yields

$$D_{\mathrm{procedure}} = \frac{1}{1 + \frac{\alpha_{\mathrm{heat}}}{\alpha_{\mathrm{cool}}}}. \tag{3}$$

The best MRN performance would be obtained when $D_{\mathrm{procedure}}$ is equal to 100%, i.e., the coil can operate in dc-mode. While IGC can work in dc-mode with low duty cycle gradient pulses [21], it should be kept in mind that decreasing D_{sequence} also decreases the number of injections per second, thus extending the duration of the procedure.

Better performance can be reached when working at the highest admissible temperature range. Indeed, the Newton law of temperature states that the cooling rate is directly proportional to the difference between the coil temperature and the cooling fluid temperature. Such behavior can be seen on the exponential decay of the temperature at the end of the stress test. Consequently, better cooling results are obtained when the difference between T_{coil} and T_{water} is the highest, i.e., at maximum admissible temperature. Furthermore, as the cooling efficiency is increased at high temperature, the heating rate constant is also smaller, thus further increasing the available propulsion time. This effect can be clearly seen in Table IV: the heating rate of the first heating pulse is higher than subsequent heating periods. In the end, working at higher coil temperature is highly desirable as the cooling is more efficient, and thus, more propulsion time is available.

In addition, other factors may negatively affect the temperature response of the coil. More complex vessel architecture, for instance with 3-D orientation, will significantly change the temperature response of the coil and decrease the available propulsion time. As such, developing a theoretical framework is necessary to model the temperature behavior of the IGC for any vascular network and any gradient sequence.

Finally, to further improve MRN efficiency, we can take advantage of cooling time to run imaging sequences. While interleaving gradient pulses with a tracking sequence is highly desirable [7], [27], [28], in practice, this cannot be achieved when performing MRN in tiny vessels as the blood flow velocity can reach several centimeters per second [29], [30], and tracking sequences can last as long as 3 s [15]. The proposed approach is different as we interleave burst-mode propulsion phases with imaging routines (see Fig. 7) to gather information during the procedure about the particle distribution and potentially readjust propulsion parameters—since the blood flow may change during the procedure [31]. Moreover, imaging sequences are low duty cycle routines; for instance, using our IGC, the magnetic signature selective excitation tracking sequence [11] has a duty cycle of 20% and a maximum gradient amplitude of 20%. A more complex sequence such as the 3-D gradient echo can be

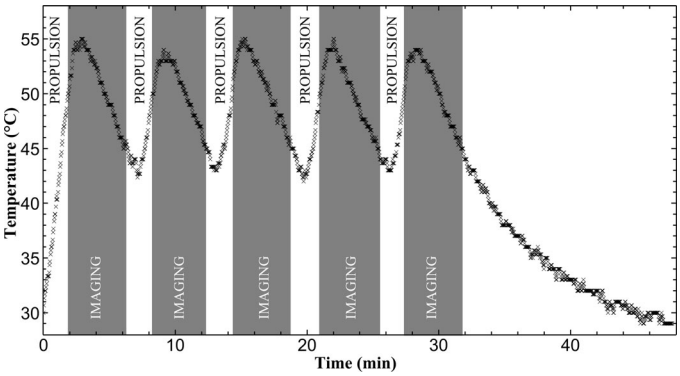

Fig. 7. Interleaving propulsion sequences with imaging sequences takes advantage of the cooling dead time to evaluate the particle distribution during the procedure without increasing the coil temperature. When a steady-state temperature is reached, the intervention time can be extended at any time during the procedure to deliver a higher drug dose.

performed with our IGC using a duty cycle of 18% and mean gradient amplitude of 25%. Running such sequences on the IGC did not increase the coil inner temperature and can thus be performed during cooling phases with no performance loss.

V. Conclusion

While MRN was previously constrained to single bifurcation steering because of limited hardware performance, we successfully demonstrated that IGC can be used for multiple bifurcation navigation as it provides both high gradient amplitude and high slew rate. Navigation of a bead through three consecutive channels has been demonstrated *in vitro*, and results indicate that MRN along a higher number of consecutive branches is possible. IGC temperature test showed that the system can sustain a long propulsion procedure where navigation periods are interleaved with cooling periods. Particle distribution assessment can be performed without observable coil temperature rise during the cooling period. Future work will focus on the possibility of navigating beads in 3-D phantoms with more bifurcations. Theoretical framework to predict MRN-assisted interventions performance is also under development.

Appendix

The magnetophoretic velocity U_{mag} of a particle of radius R can be derived using mechanics and magnetostatics [32]. While one can safely assume that velocity is constant for micrometer-sized particles—acceleration cancels after few microseconds—it is not the case for millimeter-sized beads. As such, the bead acceleration cannot be neglected. Assuming no net flow and no friction forces between the bead and the phantom, the acceleration a of a bead of mass m_{part} is

$$m_{\mathrm{part}}\mathrm{a} = \mathrm{F}_{\mathrm{mag}} + \mathrm{F}_{\mathrm{drag}} + \mathrm{F}_{\mathrm{gravity}} + \mathrm{F}_{\mathrm{buoyancy}} \qquad (4)$$

where $\mathrm{F}_{\mathrm{mag}}$, $\mathrm{F}_{\mathrm{drag}}$, $\mathrm{F}_{\mathrm{gravity}}$, and $\mathrm{F}_{\mathrm{buoyancy}}$ are, respectively, the magnetic force, the Stokes drag force, the gravity, and the buoyancy force. Projecting (3) on the x- and z-axes—as the net velocity along y is zero—it yields the following set of differential equations:

$$\begin{aligned} m_{\mathrm{part}}a_x &= F^x_{\mathrm{mag}} - F^x_{\mathrm{drag}} \\ m_{\mathrm{part}}a_z &= F^z_{\mathrm{mag}} - F^z_{\mathrm{drag}}. \end{aligned} \qquad (5)$$

Due to the strong magnetic field inside the MRI, one can assume that the magnetization of the bead is constant, equal to M_{sat}, and oriented along z [32]. Stokes' drag force for a spherical particle of radius R_{part} immersed in a fluid of viscosity η is given by $6\pi\eta v$, v being the velocity of the particle. Finally, the equations of motion are

$$\begin{aligned} m\frac{\mathrm{d}v_x}{\mathrm{dt}} &= M_{\mathrm{sat}}V_{\mathrm{part}}G_x - 6\pi\eta R_{\mathrm{part}}v_x(t) \\ m\frac{\mathrm{d}v_z}{\mathrm{dt}} &= M_{\mathrm{sat}}V_{\mathrm{part}}G_z - 6\pi\eta R_{\mathrm{part}}v_z(t) \end{aligned} \qquad (6)$$

where V_{part} is the volume of the particle. Solving (5) with the initial conditions $v_x = v_z = 0$ yields

$$\begin{aligned} v_x &= v^x_{\mathrm{terminal}}\left[1 - \exp\left(-\frac{t}{\tau}\right)\right] \\ v_z &= v^z_{\mathrm{terminal}}\left[1 - \exp\left(-\frac{t}{\tau}\right)\right] \end{aligned} \qquad (7)$$

where the time constant τ [s] is defined as $(6\pi\eta R_{\mathrm{part}})/m$ and the terminal velocity $v^{x,z}_{\mathrm{terminal}}$ [m·s^{-1}] as $(M_{\mathrm{sat}}V_{\mathrm{part}}G_{x,z})/(6\pi\eta R_{\mathrm{part}})$. Taking $m_{\mathrm{part}} = 4.10 \times 10^{-6}$kg, it gives: $\tau = 2.3$ s, $v^x_{\mathrm{terminal}} = 2.08$ m·s^{-1}, and $v^z_{\mathrm{terminal}} = 2.27$ m·s^{-1}. We can see here that the value of the time constant is of the order of the second and confirms our hypothesis that acceleration cannot be neglected for millimeter-sized beads.

References

[1] C. T. Harris, W. B. Handler, and B. A. Chronik, "Design study to investigate the effect of curvature on gradient coil performance for localized regions of interest," *Concepts Magn. Reson.*, vol. 41B, no. 2, pp. 62–71, Apr. 2012.

[2] D. Mayer, N. M. Zahr, E. Adalsteinsson, B. Rutt, E. V Sullivan, and A. Pfefferbaum, "*In vivo* fiber tracking in the rat brain on a clinical 3 T MRI system using a high strength insert gradient coil," *Neuroimage*, vol. 35, no. 3, pp. 1077–1085, Apr. 2007.

[3] B. A. Chronik, A. Alejski, and B. K. Rutt, "Design and fabrication of a three-axis edge ROU head and neck gradient coil," *Magn. Reson. Med.*, vol. 44, no. 6, pp. 955–963, Dec. 2000.

[4] K. C. Goodrich, J. R. Hadley, S. M. Moon, B. A. Chronik, T. J. Scholl, J. T. Debever, and D. L. Parker, "Design, fabrication, and testing of an insertable double-imaging-region gradient coil," *Concepts Magn. Reson.*, vol. 35B, no. 2, pp. 98–105, Apr. 2009.

[5] J.-B. Mathieu, G. Beaudoin, and S. Martel, "Method of propulsion of a ferromagnetic core in the cardiovascular system through magnetic gradients generated by an MRI system," *IEEE Trans. Biomed. Eng.*, vol. 53, no. 2, pp. 292–299, Feb. 2006.

[6] J.-B. Mathieu, S.-K. Lee, E. G. Budesheim, Y. Hua, J. Lin, C. Immer, S. M. Lechner-Greite, J. Piel, J. F. Schenck, M. A. Bernstein, J. Huston, and T. K. Foo, "Preliminary evaluation of a high performance gradient coil for 3T head specialty scanner," presented at the Int. Soc. Magn. Reson. Med. Conf., Salt Lake City, UT, USA, 2013.

[7] S. Martel, J.-B. Mathieu, O. Felfoul, A. Chanu, E. Aboussouan, S. Tamaz, P. Pouponneau, L. Yahia, G. Beaudoin, G. Soulez, and M. Mankiewicz, "A computer-assisted protocol for endovascular target interventions using a clinical MRI system for controlling untethered microdevices and future nanorobots," *Comput. Aided Surg.*, vol. 13, no. 6, pp. 340–352, Nov. 2008.

[8] J.-B. Mathieu and S. Martel, "Magnetic microparticle steering within the constraints of an MRI system: Proof of concept of a novel targeting approach," *Biomed. Microdevices*, vol. 9, no. 6, pp. 801–808, Dec. 2007.

[9] P. Pouponneau, J.-C. Leroux, and S. Martel, "Magnetic nanoparticles encapsulated into biodegradable microparticles steered with an upgraded magnetic resonance imaging system for tumor chemoembolization," *Biomaterials*, vol. 30, no. 31, pp. 6327–6332, Oct. 2009.
[10] S. N. Tabatabaei, S. Duchemin, H. Girouard, and S. Martel, "Towards MR-navigable nanorobotic carriers for drug delivery into the brain," in *Proc. IEEE Int. Conf. Robot. Autom.*, May 2012, pp. 727–732.
[11] O. Felfoul, J. B. Mathieu, G. Beaudoin, and S. Martel, "*In vivo* MR-tracking based on magnetic signature selective excitation," *IEEE Trans. Med. Imag.*, vol. 27, no. 1, pp. 28–35, Jan. 2008.
[12] P. Pouponneau, J. C. Leroux, G. Soulez, L. Gaboury, and S. Martel, "Co-encapsulation of magnetic nanoparticles and doxorubicin into biodegradable microcarriers for deep tissue targeting by vascular MRI navigation," *Biomaterials*, vol. 32, no. 13, pp. 3481–3486, May 2011.
[13] E. Diller and M. Sitti, "Micro-scale mobile robotics," *Found. Trends Robot.*, vol. 2, no. 3, pp. 117–259, 2011.
[14] S. Martel, "Magnetic navigation control of microagents in the vascular network: Challenges and strategies for endovascular magnetic navigation control of microscale drug delivery carriers," *IEEE Control Syst.*, vol. 33, no. 6, pp. 119–134, Dec. 2013.
[15] S. Martel, "Microrobotics in the vascular network: Present status and next challenges," *J. Micro-Bio Robot.*, vol. 8, no. 1, pp. 41–52, Feb. 2013.
[16] M. P. Kummer, J. J. Abbott, B. E. Kratochvil, R. Borer, A. Sengul, and B. J. Nelson, "OctoMag: An electromagnetic system for 5-DOF wireless micromanipulation," in *Proc. IEEE Int. Conf. Robot. Autom.*, May 2010, pp. 1610–1616.
[17] S. Schuerle, S. Erni, M. Flink, B. E. Kratochvil, and B. J. Nelson, "Three-dimensional magnetic manipulation of micro- and nanostructures for applications in life sciences," *IEEE Trans. Magn.*, vol. 49, no. 1, pp. 321–330, Jan. 2013.
[18] S. Martel, J.-B. Mathieu, O. Felfoul, A. Chanu, E. Aboussouan, S. Tamaz, P. Pouponneau, L. Yahia, G. Beaudoin, G. Soulez, and M. Mankiewicz, "Automatic navigation of an untethered device in the artery of a living animal using a conventional clinical magnetic resonance imaging system," *Appl. Phys. Lett.*, vol. 10, no. 1, pp. 144–152, 2007.
[19] J.-B. Mathieu and S. Martel, "Steering of aggregating magnetic microparticles using propulsion gradients coils in an MRI Scanner," *Magn. Reson. Med.*, vol. 63, no. 5, pp. 1336–1345, May 2010.
[20] V. Lalande, F. P. Gosselin, and S. Martel, "Catheter steering using a magnetic resonance imaging system," in *Proc. IEEE Eng. Med. Biol. Soc. Conf.*, Buenos Aires, Argentina, 2010, pp. 1874–1877.
[21] S. Martel, "Combining pulsed and DC gradients in a clinical MRI-based microrobotic platform to guide therapeutic magnetic agents in the vascular network," *Int. J. Adv. Robot. Syst.*, vol. 10, 2013.
[22] R. Kimmlingen, E. Eberlein, P. Dietz, S. Kreher, J. Schuster, J. Riegler, V. Matschl, V. Schnetter, A. Schmidt, E. Mustafa, D. Fischer, A. Potthast, L. Kreischer, M. Eberler, F. Hebrank, H. Thein, K. Heberlein, P. Hoecht, T. Witzel, D. Tisdall, J. Xu, E. Yacoub, G. Adriany, E. Auerbach, S. Moeller, D. Feinberg, D. Lehne, L. Lawrence, B. Rosen, K. Ugurbil, D. Van Essen, V. Wedeen, and F. Schmitt, "Concept and realization of high strength gradients for the Human Connectome Project," presented at the Int. Soc. Magn. Reson. Med. Conf., Melbourne, Australia, 2012.
[23] M. Vonthron, V. Lalande, and S. Martel, "A MRI-based platform for catheter navigation," in *Proc. IEEE Eng. Med. Biol. Soc. Conf.*, Boston, MA, USA, 2011, pp. 5392–5395.
[24] N. Olamaei, F. Cheriet, and S. Martel, "Accurate positioning of magnetic microparticles beyond the spatial resolution of clinical MRI scanners using susceptibility artifacts," in *Proc. IEEE Eng. Med. Biol. Soc. Conf.*, Jan. 2011, pp. 2800–2803.
[25] S. Martel, "Signal and image processing in medical nanorobotics: The art of tracking and imaging therapeutics navigated in the vascular network towards the region to be treated," in *Proc. 11th Int. Conf. Inf. Sci., Signal Process. Appl.*, 2012, pp. 611–617.
[26] D. Folio, C. Dahmen, T. Wortmann, M. A. Zeeshan, K. Shou, S. Pané, B. J. Nelson, A. Ferreira, and S. Fatikow, "MRI magnetic signature imaging, tracking, and navigation for targeted micro/nanocapsule therapeutics," in *Proc. IEEE/RSJ Int. Conf. Intell. Robot. Syst.*, 2011, pp. 1297–1303.
[27] S. Martel, J.-B. Mathieu, O. Felfoul, A. Chanu, E. Aboussouan, S. Tamaz, P. Pouponneau, L. Yahia, G. Beaudoin, G. Soulez, and M. Mankiewicz, "Automatic navigation of an untethered device in the artery of a living animal using a conventional clinical magnetic resonance imaging system," *Appl. Phys. Lett.*, vol. 90, no. 11, pp. 114103–114105, Mar. 2007.
[28] S. Tamaz, R. Gourdeau, A. Chanu, J.-B. Mathieu, and S. Martel, "Real-time MRI-based control of a ferromagnetic core for endovascular navigation," *IEEE Trans. Biomed. Eng.*, vol. 55, no. 7, pp. 1854–1863, Jul. 2008.
[29] T. Yzet, R. Bouzerar, J.-D. Allart, F. Demuynck, C. Legallais, B. Robert, H. Deramond, M.-E. Meyer, and O. Balédent, "Hepatic vascular flow measurements by phase contrast MRI and Doppler echography: a comparative and reproducibility study," *J. Magn. Reson. Imag.*, vol. 31, no. 3, pp. 579–588, Mar. 2010.
[30] G. G. H. Hübner, N. Steudel, G. Kleber, C. Behrmann, E. Lotterer, and W. E. Fleig, "Hepatic arterial blood flow velocities: Assessment by transcutaneous and intravascular Doppler sonography," *J. Hepatol.*, vol. 32, no. 6, pp. 893–899, Jun. 2000.
[31] R. López-Benítez, G. M. Richter, H.-U. Kauczor, S. Stampfl, J. Kladeck, B. A. Radeleff, M. Neukamm, and P. J. Hallscheidt, "Analysis of nontarget embolization mechanisms during embolization and chemoembolization procedures," *Cardiovasc. Intervention Radiol.*, vol. 32, no. 4, pp. 615–622, Jul. 2009.
[32] G. Vidal and S. Martel, "Measuring the magnetophoretic characteristics of magnetic agents for targeted diagnostic or therapeutic interventions in the vascular network," *J. Micro-Bio Robot.*, vol. 8, no. 2, pp. 65–71, Apr. 2013.

Alexandre Bigot received the B.Sc. and M.S degrees in physics applied to micro- and nanotechnologies from the Grenoble Institute of Technology, PHELMA, Grenoble, France, in 2007 and in 2009, respectively. He is currently working toward the Ph.D. degree with the Nanorobotics Laboratory, Department of Biomedical Engineering, Polytechnique Montreal, Montreal, QC, Canada, and with the Centre Hospitalier de l'Université de Montréal, Department of Radiology.

His research interests include the development of strategies for the navigation of microdevices using the gradients generated by magnetic resonance imaging scanners and the study of ultrahigh magnetic gradient systems in magnetic resonance imaging.

Charles Tremblay was born in Montreal, QC, Canada, in 1979. He received the B.S. degree in physic engineering from Polytechnique Montreal, in 2003.

From 2004 to 2013, he was a Research Associate with the Polytechnique Montreal NanoRobotics Laboratory. Since 2013, he is a Research Adviser and Infrastructure Project Manager with Polytechnique Montreal. He has published several papers, and his research interests include microfluidics, magnetic resonance imaging antennaes, robotics systems, microscopy, multiphotons, 3-D direct nanoprinting, and magnetotactic bacteria.

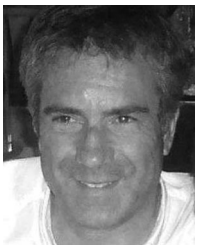

Gilles Soulez completed medical and doctoral studies in Paris, France, receiving the MD, M.Sc., and FRCPC degree.

He completed his radiology residency at the University Paris V in 1988 and completed a two-year fellowship combined with a certification of the French College of Interventional Radiology from the University Paris VII and VI and the diploma degree in magnetic resonance imaging from the University Paris XI. He was certified in radiology in Montreal, QC, Canada, in 1992 and was recruited as a Vascular and Interventional Radiologist with the Centre Hospitalier de l'Université de Montréal. He is currently a Professor of radiology and the Director of the Department of Radiology, Radiation-Oncology and Nuclear Medicine, University of Montreal. His research is dedicated to the advancement of vascular and interventional radiology and is funded by the Canadian Fund of Innovation, Canadian Institute of Health Research, Natural Science and Engineering Research Council, Fonds de la Recherché en Santé du Québec (FRSQ). He has published more than 133 peer-reviewed papers during his career and holds eight patents.

Dr. Soulez received the National Scientist Award from the FRSQ.

Sylvain Martel (SM'07) received the Ph.D. degree in electrical engineering from Institute of Biomedical Engineering, McGill University, Montréal, QC, Canada, in 1997.

Following Postdoctoral studies at the Massachusetts Institute of Technology (MIT), Cambridge, MA, USA, he was appointed as a Research Scientist with the BioInstrumentation Laboratory, Department of Mechanical Engineering, MIT. From February 2001 to September 2004, he had dual appointments at MIT and was an Assistant Professor with the Department of Electrical and Computer Engineering and the Institute of Biomedical Engineering, Polytechnique Montréal, Campus of the University of Montréal. He is currently a Professor with the Department of Computer and Software Engineering and the Institute of Biomedical Engineering and the Director of the NanoRobotics Laboratory, Polytechnique Montréal, which he founded in 2002. He is a Fellow of the Canadian Academy of Engineering and held the Canada Research Chair in micro/nanosystem development, fabrication, and validation, from 2001 to 2010, prior to obtaining the Polytechnique Research Chair in nanorobotics. In the medical field alone, he pioneered several innovative technologies such as the first parallel computing platform for remote surgeries, direct cardiac mapping systems designed to investigate the cause of sudden cardiac deaths, and new brain implants for decoding neuronal activities in the motor cortex. Currently, he is leading an interdisciplinary team involved in the development of new types of therapeutic agents and interventional platforms for cancer therapy.